Nanotechnology, Nanomaterials

Templated Self-Assembly of Block Copolymer Thin Films Under Lithographic Confinement

H. Do, H. Choi, J. Chang, C. A. Ross, K. K. Berggren

Sponsorship: National Science Foundation, Taiwan Semiconductor Manufacturing Company

Physical or chemical templates can direct the self-assembly of block copolymers (BCPs) to achieve well-aligned nanoscale patterns. Complex patterns have previously been demonstrated using a sparse array of lithographically defined and chemically functionalized posts. However, self-assembly of BCPs confined within a topographic template fabricated by electron-beam lithography has not been studied in detail. In this work, we describe how physical confinement affects the self-assembly of cylindrical-phase polystyrene-*b*-polydimethylsiloxane (PS-*b*-PDMS) BCP thin films. This work could lead to a new pattern-generation technique that enables high-throughput pattern generation.

We used an array of square-grid templates fabricated by electron-beam lithography using hydrogen silesquioxane (HSQ) resist. The patterned substrate was treated with a hydroxyl-terminated PS brush layer. PS-*b*-PDMS block copolymer (45.5 kg/mol) was spin cast on the template and solvent annealed in a 5:1 mixture of toluene and heptane for 3 h at room temperature. The top PDMS layer and PS matrix were removed by CF_4 and O_2 reactive-ion etching, respectively. As shown in Figure 1, PDMS microdomains formed a bar-shaped structure when confined inside a square grid. The bar-shaped structures were randomly aligned to the horizontal and vertical directions because the size of the grid was equal in both directions. In Figure 1(a), 18 structures were aligned horizontally and 18 structures were aligned vertically. As the size of the square was increased, some bar-shaped structures were not fully connected. In Figure 1(b), such defects are visible. One additional bar was formed inside each square compared to the structures in Figure 1(a).

We fabricated a rectangular grid array to control the alignment of the bar-shaped structures. Bar-shaped PDMS structures similar to those shown in Figure 1(a-b) were produced, but now with horizontal alignment. Figures 2(a) and 2(b) show PDMS microdomains confined within a rectangular grid array with aspect ratios of 1.3 and 1.5, respectively. The alignment direction of the bars was preferentially along the horizontal axis resulting in less T-junctions because of the high free-energy penalty associated with forming T-junctions.

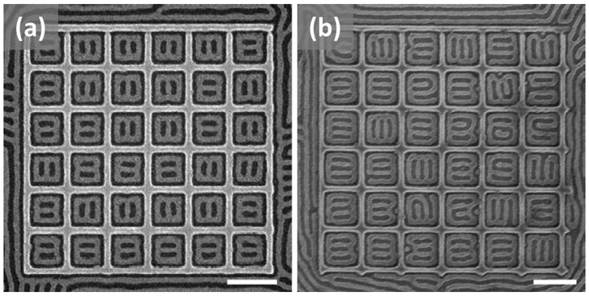

▲ Figure 1: Scanning electron microscope (SEM) images of PDMS microdomains confined inside a square grid array. Size of the square grid was (a) 140 nm and (b) 160 nm. All scale bars are 200 nm in length. (a) The PDMS microdomains formed bar-shaped structures with two T-junctions in each structure. Alignment direction of the structure was random. (b) The PDMS microdomains formed bar-shaped structures with four T-junctions in each structure. Several defects were observed. White lines are oxidized HSQ, and gray lines are oxidized PDMS microdomains.

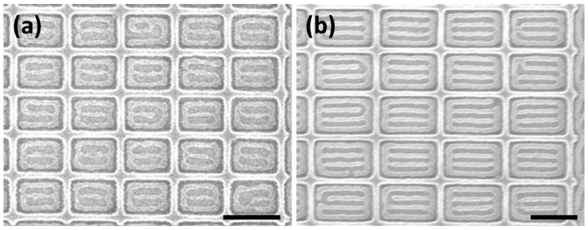

▲ Figure 2: SEM images of PDMS microdomains confined inside a rectangular grid array. Widths of the rectangular grids were (a) 160 nm and (b) 250 nm. All scale bars are 200 nm in length. (a) The PDMS microdomains formed bar-shaped structures that were horizontally aligned. Two T-junctions were formed in each structure. (b) The bar-shaped structures were aligned horizontally, and four T-junctions were formed in each structure. For both cases, the structures were aligned horizontally to reduce the number of T-junctions and therefore minimize free energy. Aspect ratios were (a) 1.3 and (b) 1.5.

FURTHER READING

- J. K. W. Yang, Y. Jung, J. Chang, R. A. Mickiewicz, A. Alexander-Katz, C. A. Ross, and K. K. Berggren, "Complex Self-Assembled Patterns using Sparse Commensurate Templates with Locally Varying Motifs," *Nat. Nanotechnol.*, vol. 5, pp. 256-260, 2010.
- A. Tavakkoli K. G., K. W. Gotrik, A. F. Hannon, A. Alexander-Katz, C. A. Ross, and K. K. Berggren, "Templating Three-Dimensional Self-Assembled Structures in Bilayer Block Copolymer Films," *Science,* vol. 336, pp. 1294-1298, 2012.

Lithographic Control of Surface and Volume Plasmons in Aluminum

R. G. Hobbs, V. R. Manfrinato, Y. Yang, S. A. Goodman, L. Zhang , D. Su, E. A. Stach, K. K. Berggren

Sponsorship: EFRC Center for Excitonics, Brookhaven National Laboratory, Gordon and Betty Moore Foundation

Aluminum has garnered significant attention as a plasmonic material recently due to the fact that its material properties support surface plasmon (SP) resonances across the entire visible spectrum and deep into the ultraviolet. Moreover, the volume plasmon (VP) resonance in Al has been exploited recently to measure the valence electron density, and by interpolation the material temperature, of an active Al microelectronic device, locally, on the nanoscale. Consequently, the control of plasmonic modes in Al nanostructures is of major interest for applications from nano-optical devices operating in the UV region of the electromagnetic spectrum to nanoscale thermal measurements in active electronic or optoelectronic devices.

In this work we have demonstrated the lithographic control of plasmonic modes in Al nanostructures fabricated by electron-beam lithography (EBL) on ultrathin, 5-10 nm thick SiN$_x$ membranes. We used spatially resolved electron energy-loss spectroscopy (EELS) to map plasmonic modes in Al nanostructures. EELS measurements were performed using the aberration-corrected Hitachi STEM at Brookhaven National Laboratory operating at 200 keV, with an energy-resolution of 400 meV and energy dispersion of 50 meV. We measured the energy and lifetime of SP and VP modes in Al nanodisks as a function of nanodisk diameter, and simulations and models have been shown to accurately reflect the observed relationship between nanodisk diameter and SP/VP characteristics. Figure 1 shows the results of experiments to spatially map surface plasmon excitations in Al nanodisks.

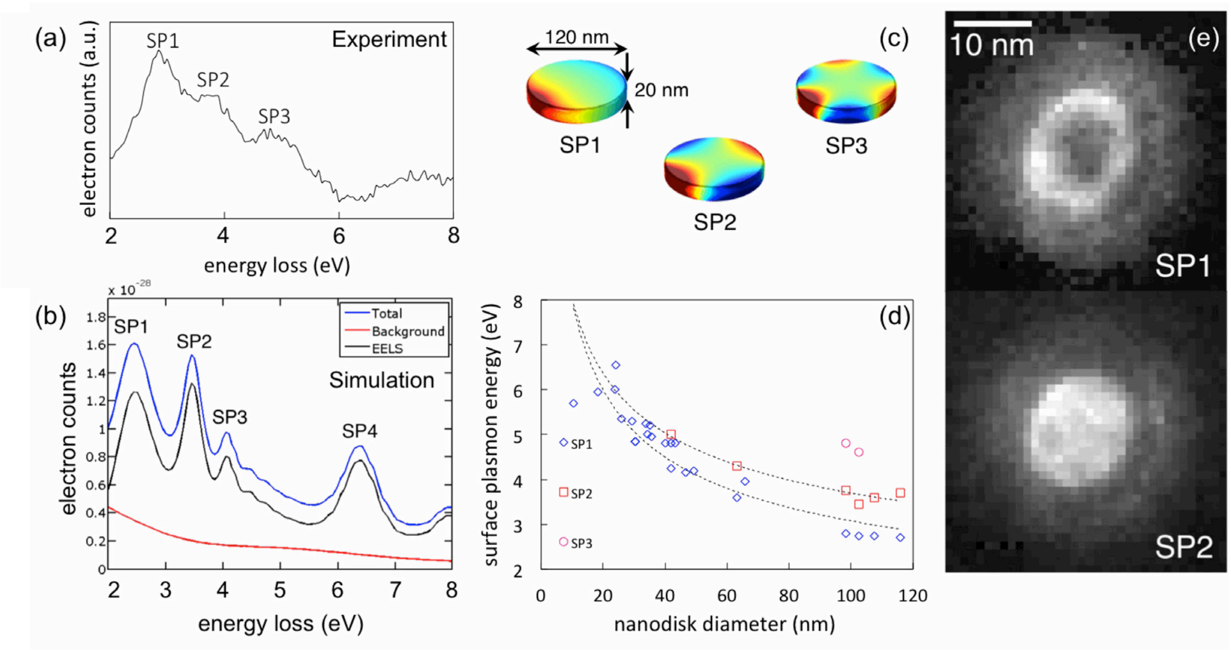

▲ Figure 1: Lithographic control of surface plasmons (SPs) in Al nanodisks. (a) Experimentally measured EEL spectrum for a 120 nm diameter Al nanodisk. The measured spectrum is in excellent agreement with the simulated spectrum in (b). (c) Maps of electric field intensity at the surface of a 120 nm diameter Al nanodisk for the three lowest energy SP modes: SP1, SP2, and SP3, which represent dipolar, quadrupolar, and hexapolar modes, respectively. (d) Plot of SP energy against nanodisk diameter for SP1, SP2, and SP3 surface plasmon modes. (e) EEL maps recorded at energy-loss of SP1 and SP2 modes, respectively, in a 12 nm diameter Al nanodisk.

FURTHER READING

- M. W. Knight, N. S. King, L. Liu, H. O. Everitt, P. Nordlander, and N. J. Halas, "Aluminum for plasmonics," *ACS Nano*, vol. 8, pp. 834-840, 2014.
- V. R. Manfrinato, J. Wen, L. Zhang, Y. Yang, R. G. Hobbs, B. Baker, D. Su, D. Zakharov, N. J. Zaluzec, D. J. Miller, E. A. Stach, and K. K. Berggren, "Determining the resolution limits of electron-beam lithography: direct measurement of the point-spread function," *Nano Letters*, vol. 14, pp. 4406-4412, 2014.
- R. G. Hobbs, Y. Yang, A. Fallahi, P. D. Keathley, E. De Leo, F. X. Kärtner, W. S. Graves, and K. K. Berggren, "High-Yield, Ultrafast, Surface Plasmon-Enhanced, Au Nanorod Optical Field Electron Emitter Arrays," *ACS Nano*, vol. 8, pp. 11474-11482, 2014.

Interaction-Free Measurement by Three-Crystal Electron Interferometer

C. S. Kim, Y. Yang, V. R. Manfrinato, R. G. Hobbs, A. Agarwal, K. K. Berggren
Sponsorship: Gordon and Betty Moore Foundation

Non-destructive imaging of biological samples has been a much sought-after goal in the field of electron microscopy. The quantum electron microscope (QEM) comprising two quantum mechanically coupled electron beams was proposed in 2009 as a means of achieving this goal. A major challenge in the proof of the QEM concept is the demonstration of an interaction-free measurement (IFM) with electrons.

We are investigating a Marton-type electron interferometer (Figure 1(a)) to achieve IFM in a standard transmission electron microscope (TEM). This device consists of three crystal gratings that split and recombine the incident electron beam via diffraction. IFM of an object placed across one of these beams (the sample beam) can be achieved analogous to previously demonstrated IFM with photons in a Mach-Zehnder interferometer geometry.

We used focused gallium ion beam milling (FIB) to fabricate a two-crystal grating from a single silicon crystal monolith. The interferometer has to be precisely aligned due to the short wavelength of the electron (2.5 pm at 200 keV). Using FIB ensures that each grating has the same crystal orientation. We investigated the effect of grating thickness on the fraction of electrons lost through decoherence using electron energy loss spectroscopy. We also fabricated a three-crystal grating structure (Figure 1(b)) as a first step toward the Marton-type interferometer. This structure was used to study diffraction (Figure 1(c)) and interference of the electron beam. We carried out optimization of the interferometer design parameters (diameter of the incident beam, separation between crystal layers) and effects of misalignment (crystal rotation and translation) on the interference fringes.

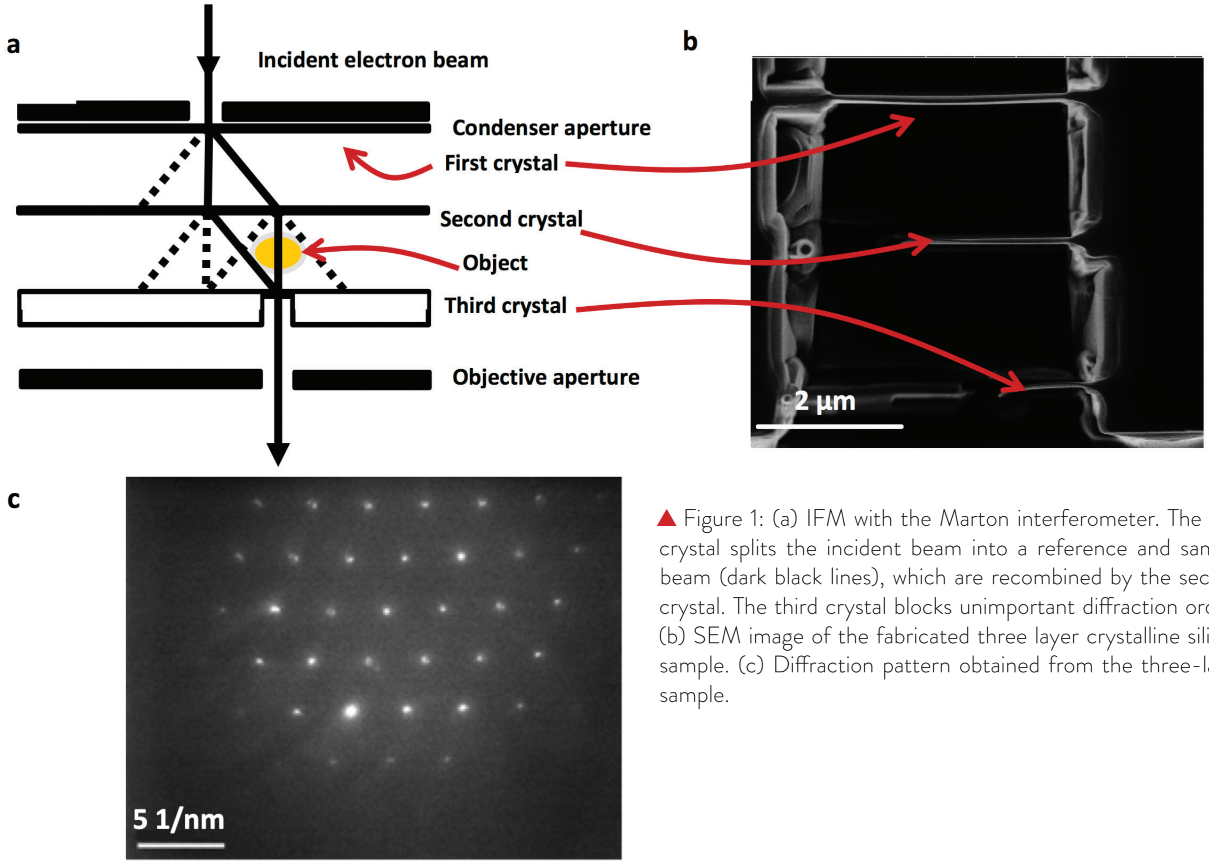

▲ Figure 1: (a) IFM with the Marton interferometer. The first crystal splits the incident beam into a reference and sample beam (dark black lines), which are recombined by the second crystal. The third crystal blocks unimportant diffraction orders. (b) SEM image of the fabricated three layer crystalline silicon sample. (c) Diffraction pattern obtained from the three-layer sample.

FURTHER READING

- W. P. Putnam and M. F. Yanik, "Noninvasive electron microscopy with interaction-free quantum measurements" *Phys. Rev. A*, vol. 80, pp. 040902R, 2009.
- L. Marton, "Electron Interferometer," *Phys. Rev.*, vol. 85, pp. 1057-1058, 1952.
- A. G. White, J. R. Mitchell, O. Nairz and P. G. Kwiat, "'Interaction-Free' Imaging" *Phys. Rev. A*, vol. 58, pp. 605-613, 1998.

Membrane Nano-Gratings for Electron Diffraction

Y. Yang, R. Hobbs, V. Manfrinato, C. Kim, O. Celiker, A. Agarwal, K. K. Berggren
Sponsorship: Gordon and Betty Moore Foundation

Nanofabricated electron beam transmission gratings are of interest for a variety of applications, such as electron interferometry, electron holography, and electron vortex beam generation. Compared with natural crystalline samples as electron diffraction "gratings," nano-fabricated gratings provide more flexibility on the control of diffraction angle and orbital angular momentum of diffracted electron beams and can be used with various electron energies. Here we report ~10-nm-thick membrane silicon nitride nano-gratings fabricated with electron beam lithography (EBL) and characterized with electron diffraction in a transmission electron microscope (TEM).

The fabrication process started with silicon nitride membrane (5-20 nm) TEM grids (purchased from *SiMPore Inc.*). Oxygen plasma ashing was applied to clean the membrane and promote resist adhesion. Then, 50 nm poly-methyl-methacrylate (PMMA) electron beam resist was spin-coated on the membrane, and the nano-grating patterns were defined by an Elionix F-125 EBL system. After resist development, CF_4 reactive ion etching (RIE) transferred the pattern to the silicon nitride membrane. Two-dimensional mesh gratings (Figure 1(a)) were fabricated as it allows for large area patterning without delamination issues observed in one-dimensional line gratings. The grating pitch varied from 40 nm to 100 nm, and the patterned area ranged from 2µm to 100µm. Nano-gratings were characterized in a JEOL 2010F TEM operating in high-dispersion diffraction (HDD) mode. Compared to normal electron diffraction mode, HDD mode offered a longer camera length (up to 80 m) and thus a higher magnification to better visualize the diffraction spots located close to the central spot on the diffraction plane. In the diffraction pattern (Figure 1(b)), the diffraction spots' spacing was commensurate with the nano-grating pitch, verifying that these spots were indeed generated by electron diffraction from the nano-gratings.

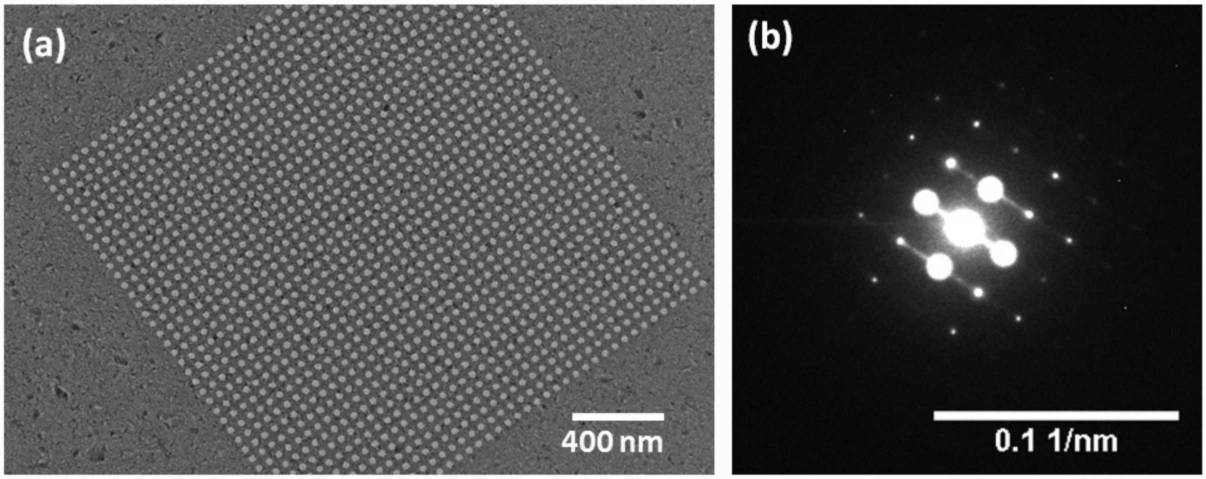

▲ Figure 1: (a) TEM image of a two-dimensional mesh grating patterned on a 10-nm-thick silicon nitride membrane with 10 nm gold coating layer. The grating pitch is 50 nm, and the patterned area is a 2 µm 2 µm square. The purpose of the gold layer is to prevent charging during imaging and diffraction. (b) A high-dispersion diffraction pattern of the mesh nano-grating recorded by JEOL 2010F TEM operating at 200 kV with 80 m camera length.

FURTHER READING

- G. Gronniger, B. Barwick, and H. Batelaan, "A three-grating electron interferometer," *New Journal of Physics*, vol. 8, p. 224, 2006.
- J. Verbeeck, H. Tian, and P. Schattschneider, "Production and application of electron vortex beams," *Nature*, vol. 467, pp. 301-304, 2010.
- B. J. McMorran, A. Agrawal, I. M. Anderson, A. A. Herzing, H. J. Lezec, J. J. McClelland, and J. Unguris, "Electron Vortex Beams with High Quanta of Orbital Angular Momentum," *Science*, vol. 331, pp. 192-195, 2011.

Slurry Abrasive Particle Agglomeration Experimentation and Modeling for Chemical Mechanical Planarization

D. S. Boning, J. Johnson

Sponsorship: SRC/SEMATECH Engineering Research Center for Environmentally Benign Semiconductor Manufacturing, Intel

A theoretical modeling approach is developed to predict silica-specific instability in chemical-mechanical polishing (CMP) slurries. In CMP, the formation of large agglomerates such as those seen in Figure 1 is of great concern, as these large particles are associated with high defectivity and poor polish performance. The proposed model describes the complex CMP slurry system as a colloid under high non-linear shear conditions. The model diverges from the classic colloidal models by focusing both on reaction-limited agglomeration (RLA) bounded by silica-specific modes of transitory bonding and on modified DVLO assumptions to include chemical activation and hydrodynamic agglomerate break-up condition evaluation. In order to build physical intuition and predict key model parameters, fundamental experimental studies and novel metrology of agglomerates are performed.

This work finds, in agreement with colloidal and interface science literature, that the specific chemical attributes of *silica* CMP slurry abrasives are the primary drivers of agglomeration, with the secondary being the mechanical application of shear forces (as seen in Figure 2). As a result, we have built both an empirically intuitive and theoretically fundamental model for understanding the behavior of these particles in contrast to other oxide particles, as well as their chemical and hydrodynamic properties under the shear caused by CMP.

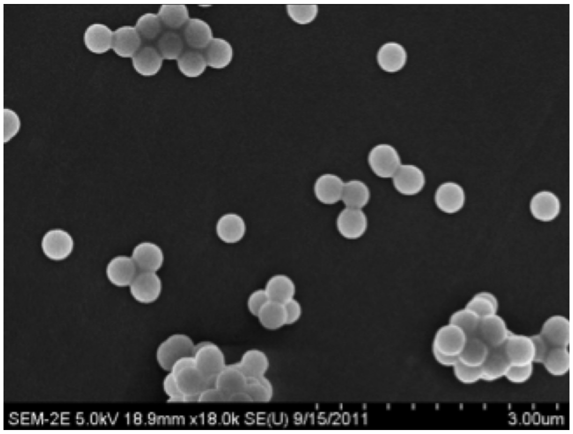

▲ Figure 1: SEM of slurry particle agglomerates arising in systematic CMP experiments.

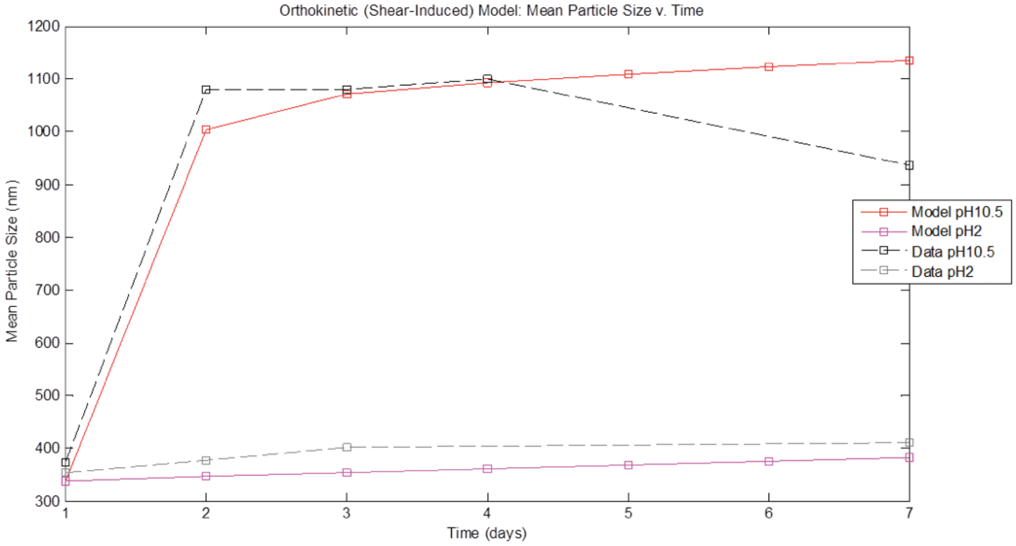

▲ Figure 2: Comparison of model and experimental data for agglomerate growth vs. time, accounting for pH and hydrodynamic break up effects.

FURTHER READING

- D. Boning, J. Johnson, G.-S. Kim, and K. Knutson, “Slurry Particle Model for Chemical Mechanical Planarization (CMP),” in *Proc. Materials Research Society Spring Meeting*, Apr. 2010.

Pad-in-a-Bottle: Planarization with Suspended Polyurethane Beads and a Stiff Counterface

W. Fan, J. Johnson, Y. Zhuang, Y. Sampurno, A. Philipossian, D. S. Boning

Sponsorship: SRC Engineering Research Center for Environmentally Benign Semiconductor Manufacturing

"Pad-in-a-bottle" (PIB), an alternative to conventional chemical-mechanical planarization (CMP) is explored. In PIB, a stiff polycarbonate counterface replaces the polyurethane (PU) polishing pad, and 10–50 μm PU beads are used in conjunction with slurry and slurry particles to achieve planarization (Figure 1). Patterned wafer PIB experiments show improved dishing and erosion in STI test wafers. Based on the extraction of a new dual-material PIB model, simulations show that the primary source of reduced dishing and erosion is the use of the stiff counterface as enabled by the compliant beads.

Blanket 200 mm oxide wafers are polished at the University of Arizona on an APD-500 polisher, with 1.2 m/s sliding velocity and 3 to 5 PSI pressures. PU beads with median diameter of 15 and 35 μm are dispersed in Cabot Microelectronics SS25 slurry with surfactant Silsurf. The PU bead content is kept constant at 2 g/L. A polycarbonate counterface with concentric grooves is used. Oxide removal rates up to 150 nm/min are observed. Previous blanket wafer PIB modeling indicates that beads must be stacked (rather than monolayer dispersed) in order to achieve this usable removal rate.

Patterned SKW3-2 STI test wafers are polished using PIB at 5 PSI, for 7 and 10 min in the 15 and 35 μm bead diameter cases, respectively. A new patterned wafer PIB model is fit to measured dishing and erosion (Figure 2). The model accounts for and extracts the following parameters: bead diameter (15 or 35 μm), bead height distribution λ (0.14 μm), bead stacking α (11), effective oxide rate (61 nm/min) and selectivity to nitride (6:1), and counterface Young's modulus (1.6 GPa).

Based on the extracted model, full chip dishing and erosion simulation studies are performed to understand factors that are dominant in achieving dishing/erosion at nitride clear time, compared to conventional CMP. The stiff counterface is found to be most influential in achieving improved within-chip uniformity, as shown in Figure 3.

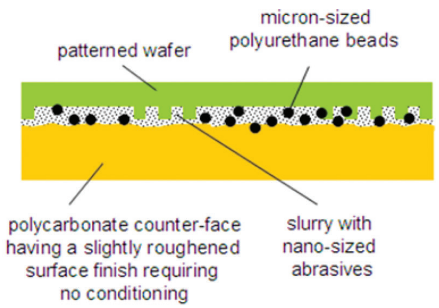

▲ Figure 1: Pad-in-a-Bottle (PIB) CMP with PU beads replacing pad asperities in conventional CMP.

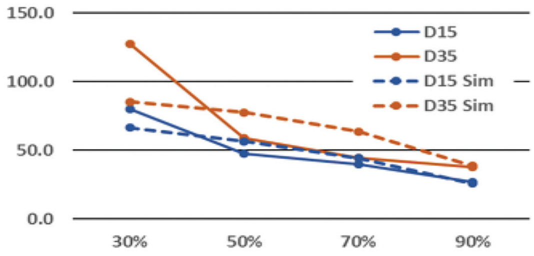

▲ Figure 2: Simulated and experimental dishing (nm) as a function of pattern density.

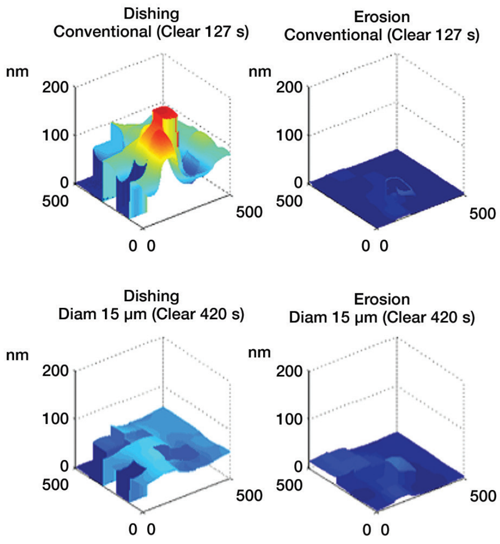

▲ Figure 3: Simulated dishing and erosion across SKW3-2 STI wafer die at nitride clear time: conventional CMP (top) and PIB (bottom).

FURTHER READING

- W. Fan, J. Johnson, and D. S. Boning, in *MRS Symp. Proc.*, vol. 1560, Mar. 2013, doi: 10.1557/opl.2013.874.

Volatile Organic Compounds Sensors based on Oxidative Chemical Vapor Deposition

X. Wang, K. K. Gleason
Sponsorship: Shell

Volatile organic compounds (VOCs) are important hazards in the petroleum industry. Many major hazardous chemicals in refineries are VOCs such as hydrocarbons and alcohol, which may lead to explosions. However, current methods to detect VOCs, such as infrared chemical detectors and transistors, require complicated fabrication methods and high cost. Therefore, it is of great importance to find an economic and efficient way to detect VOCs in refineries. Here, we demonstrate two types of chemical sensors based on oxidative chemical vapor deposition (oCVD) technology. Both chemical sensors utilize the resistance change after exposure to VOCs. The first approach is to tether metal nanoparticles on poly(3,4-ethylenedioxythiohene-co-3-thipheneacetic acid) thin films using wet chemistry. The polymer films are deposited using oCVD (Figure 1 (a)). The sensors respond to acetone/toluene/methanol by modulating the work function of the metal nanoparticles. The second approach is to use oCVD poly(3,4-ethylenedioxythiohene) coated vertically aligned carbon nanotube arrays to detect hydrocarbons. The structure is shown in Figure 1 (b), with the scanning electron microscope (SEM) images in Figure 1 (c). The response of this sensor to n-pentane is demonstrated in Figure 1 (d). Our hypothesis for the sensitivity is that the absorption of non-polar gas molecules in the p-doped conducting polymer layer will decrease the electron hopping rate in the polymer, thus changing the overall resistance. With a simple fabrication method and low cost, our sensors respond to a variety of VOCs with fast and high response.

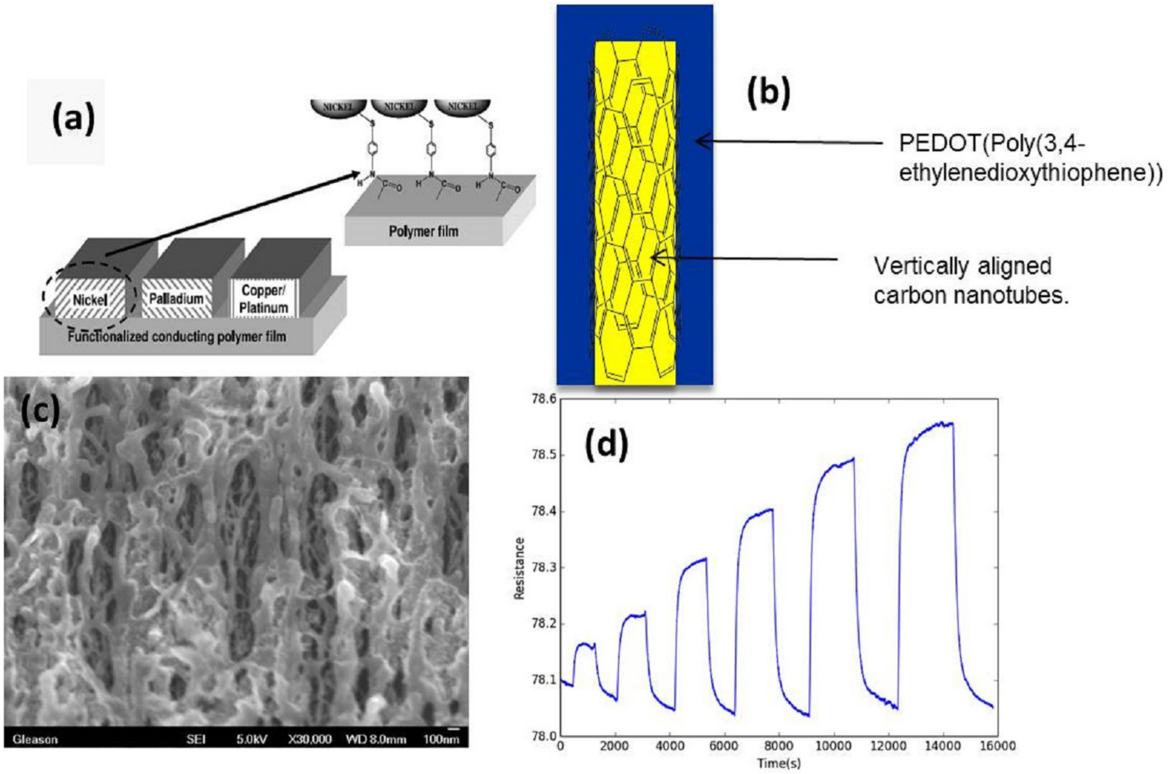

▲ Figure 1 (a) Structure of a metal nanoparticle-copolymer sensor. (b) Structure of polymer-coated carbon nanotube sensor. (c) SEM image of poly(3,4-ethylenedioxythiohene) coated carbon nanotube. (d) Response of the polymer/carbon nanotube sensor to n-pentane vapor ranging from 350 ppm to 7000 ppm.

FURTHER READING

- B. Pejcic, P. Hadington, and A. Ross, *Environmental Science & Technology*, 2007, vol. 41, no. 18, pp. 6333-6342.
- M. Barr, J. Rowehl, R. Lunt, J. Xu, A. Wang, C. Boyce, S. Im, V. Bulović, and K. Gleason, *Advanced Material*, vol. 23, pp. 3500-3505, Aug. 2011.
- S. Vaddiraju and K. K. Gleason, *Nanotechnology*, vol. 21, no. 12, p. 125503, 2010.

Strain-Engineered Manufacturing of Freeform Carbon Nanotube Microstructures

S. J. Park, M. De Volder, H. Zhao, S. Tawfick, A. J. Hart

Sponsorship: DARPA, Air Force Officer of Scientific Research, Office of Naval Research

The skins of many plants and animals have intricate micro-scale surface features that give rise to properties such as directed water repellency and adhesion, resistance to fouling, and camouflage. However, engineered mimicry of these designs has been restrained by the limited capabilities of top-down fabrication processes.

We demonstrate a new technique for scalable manufacturing of freeform microstructures via strain-engineered growth of aligned carbon nanotubes (CNTs). Offset patterning of the CNT growth catalyst and CNT growth rate modification layer is used to locally modulate the CNT growth rate. This patterning causes the CNTs to collectively bend during growth, with exceptional uniformity over large areas (Fig 1a and b). The final shape of the curved CNT microstructures can be designed via finite element modeling (FEM), and using the FEM routine, the internal stress distributions can be calculated to predict structural failure (Figure 1c and d). Because our process is based on an additive chemical synthesis process instead of a subtractive etching and release technique, it enables the direct synthesis of complex microstructures that are perpendicular rather than parallel to the substrate. This result has two major implications: it enables fabrication of closely packed arrays of structures with heterogeneous shapes, and the porosity of the CNT forests enables conformal coating after growth to modify chemical and/or mechanical properties. We demonstrate this latter point by conformal coating of CNT "microtruss" arrays by atomic layer deposition (ALD) and polymer chemical vapor deposition (CVD) which increases their mechanical stiffness without changing the geometry. This process establishes versatile principles for design and manufacturing of complex microstructured surfaces that profit from the mechanical, electrical, and thermal properties of CNTs and can leverage emerging methods for roll-to-roll micro-patterning and CVD.

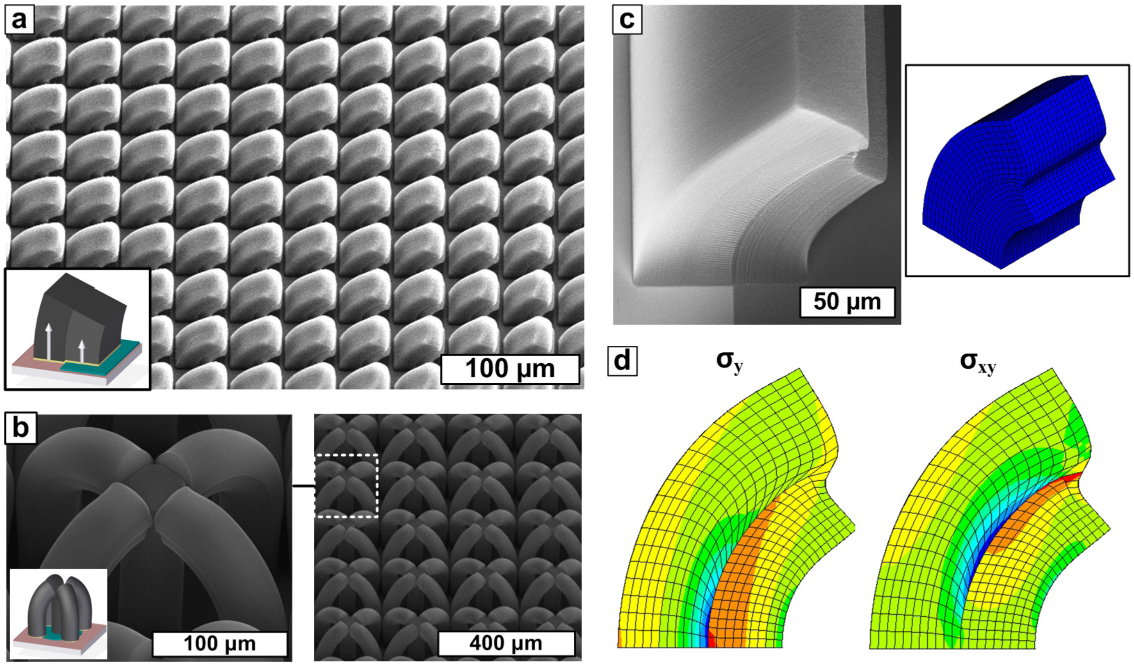

▲ Figure 1: Strain-engineered growth of 3D CNT microstructures by offset patterning of the growth catalyst on a TiN underlayer: (a) curved micropillars; (b) microtrusses. FEM simulation of strain-engineered CNT microstructure growth: (c) visual comparison of an experimentally grown structure and a simulated structure; (d) internal axial and shear stress distribution within the simulated structure.

FURTHER READING

- M. De Volder, S. J. Park, S. Tawfick, and A. J. Hart, "Strain-engineered manufacturing of freeform carbon nanotube microstructures," *Nature Communications*, vol. 5, p.4512, Jul. 2014.

Mechanism and Enhanced Yield of Carbon Nanotube Growth on Stainless Steel by Oxygen-Induced Surface Reconstruction

S. W. Pattinson, B. Viswanath, D. N. Zakharov, J. Li, E. A. Stach, A. J. Hart

Sponsorship: Pall Corporation, National Science Foundation, U.S. Department of Energy

It has been previously shown that carbon nanotubes (CNTs) can be grown directly on stainless steel (SS) alloy surfaces because SS natively contains elements that enable CNT growth following exposure to hydrocarbons at elevated temperatures (figure 1). Often CNT growth from SS surfaces has involved the use of acid immersion or oxidation in air to treat the SS surface before hydrocarbon exposure and subsequent CNT growth. However, there is no general understanding of how the surface chemistry and morphology affects the nucleation and growth of CNTs. Through environmental transmission electron microscopy (E-TEM), we observe that CNT growth is enabled by reconstruction of the SS surface following oxygen exposure at the growth temperature, followed by further break-up of the surface upon reduction, and then CNT nucleation and growth after hydrocarbon exposure (figure 2). Using electron energy loss spectroscopy (EELS), we also find that catalyst particles consist of pure iron and iron alloys such as Fe-Cr and Fe-Ni. We use these insights to study CNT synthesis on bulk net-shape porous SS materials, showing that annealing of the SS at 1000°C in air before CVD using an ethylene-based feedstock mixture results in a 70-fold increase in CNT yield. Our findings show how process conditions can be designed for efficient manufacturing of CNT-enhanced stainless steel materials and guide enhanced understanding of CNT growth on additional industrially relevant metal substrates.

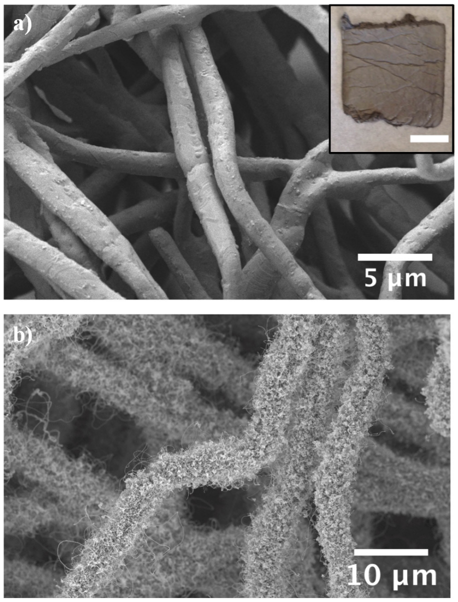

▲ Figure 1: a) SEM image of untreated SS mesh consisting of ~2 µm diameter fibers (inset: optical image with 10 mm scale bar); b) SEM image of 2 µm diameter SS fiber mesh after CNT growth.

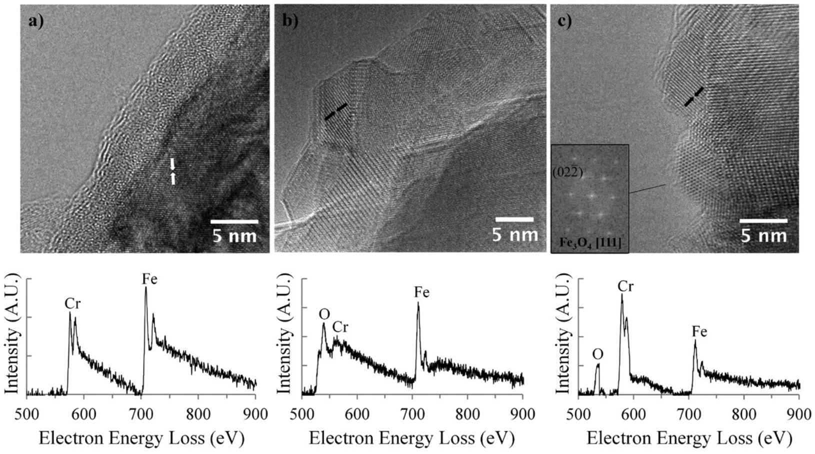

▲ Figure 2: Sequence of high-resolution TEM images and EELS spectra (with linear intensity scale) of an SS 316L surface at a) room temperature in 4×10-7 Torr vacuum (0.20nm spacing is indicated); b) in 40 mTorr oxygen at 500°C (0.34 nm spacing is indicated); c) in 4×10-7 Torr vacuum after venting oxygen but before putting in C_2H_2 and H_2, (0.27 nm spacing is indicated). Image b) was acquired by averaging 13 frames taken using the Gatan K2-IS Direct Electron Detection camera.

FURTHER READING

- S. W. Pattinson, B. Viswanath, D. N. Zakharov, J. Li, E. A. Stach, and A. J. Hart. “Mechanism and enhanced yield of carbon nanotube growth on stainless steel by oxygen-induced surface reconstruction,” *Chemistry of Materials, vol. 27, issue 3, pp. 932-937, 2015.*

High-Speed Roll-to-Roll CVD of Graphene using a Concentric Tube Reactor

E. S. Polsen (University of Michigan), D. Q. McNerny (University of Michigan), V. Balakrishnan, S. Pattinson, M. C. Feldmann, A. J. Hart

Sponsorship: National Science Foundation Scalable Nanomanufacturing Program

Continuous and scalable manufacturing techniques are crucial to enable the use of graphene in large-area applications including flexible displays and solar cells. Our group has invented and built a roll-to-roll chemical vapor deposition (CVD) machine using a novel concentric tube design, featuring a thin foil substrate that is wrapped in a helical path around the inner tube and is continuously translated and exposed to the gas atmosphere in the small gap between the concentric tubes. Radial holes in the sidewall of the inner tube enable downstream injection of the carbon source.

Through this decoupled, multi-zone reaction chamber, two sequential treatment atmospheres are seamlessly combined in a controlled thermal environment. Our research highlights the system parameters that lead to optimal quality and coverage of graphene and identifies important tradeoffs between foil translation rate and graphene quality. We demonstrate that graphene films can be produced at a foil translation speed of up to 500 mm/minute in an ethylene/hydrogen atmosphere at ~2 Torr and 1000°C. Nucleation and growth are also shown to depend strongly on substrate preparation, and annealing of the Cu foil in hydrogen prior to growth leads to ~67% increase of the graphene G/D ratio. Additionally, the concentric tube design leads to an ~90% reduction in reaction gas use as compared to typical reactors. Opportunities for further improvement of roll-to-roll graphene manufacturing include enhanced control of pre- and post-treatment atmospheres, and the integration of patterning and transfer methods as well as the integration of additional treatment zones.

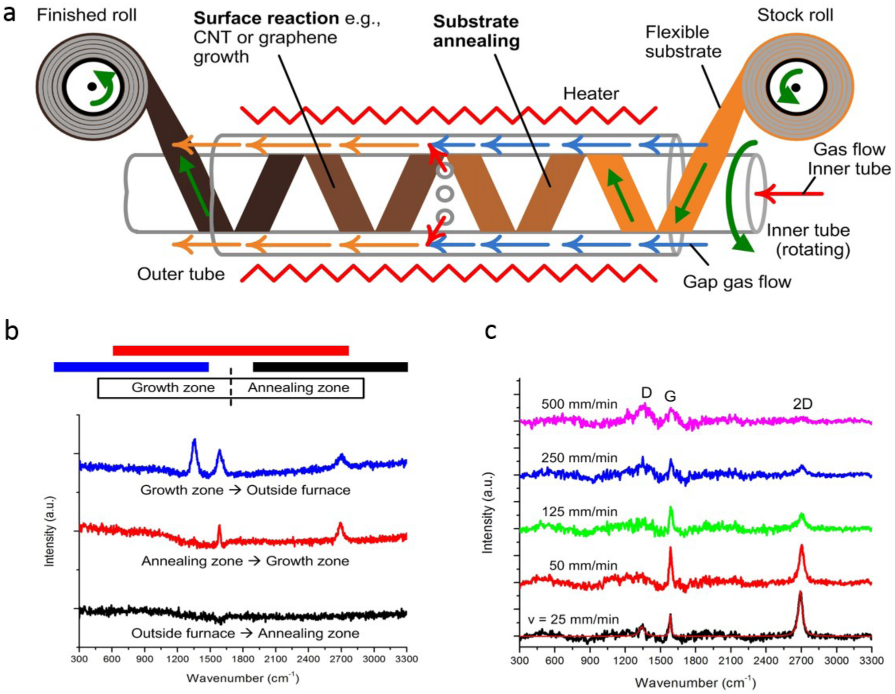

▲ Figure 1: a) Concentric tube reactor with the substrate foil wrapped around the inner tube, which carries the growth gas for the second stage of the reactor. Between the inner and outer tube flows, the gap gas anneals the substrate in the first stage of the reactor and mixes with the growth gas in the second stage. Both stages are located in a tube furnace to provide for the reaction temperature. b) Raman spectra of the substrate at points outside the furnace, in the annealing and growth zone. c) Raman spectra of graphene grown at different translation speeds.

FURTHER READING

- D. Q. McNerny, B. Viswanath, D. Copic, F. R. Laye, C. Prohoda, A. C. Brieland-Shoultz, E. S. Polsen, N. T. Dee, V. S. Veerasamy, and A. John Hart, "Direct fabrication of graphene on SiO2 enabled by thin film stress engineering," *Scientific Reports,* vol. 4, Article 5049, 23 May 2014.

Modular Robotic System for Photopatterning Large 3D Surfaces

A. Stevens, R. Oliver, L. Chin, A. J. Hart
Sponsorship: National Science Foundation, Massachusetts Institute of Technology

The capability to pattern photosensitive polymers on large curved objects, and to use these patterns to perform traditional micromachining processes, would be an enabling technology for applications including textured mold tooling and integration of electronics with custom medical implants.

Toward this goal, we have designed and built a system comprised of a 6-axis robot and a rotary stage (Figure 1a). A custom-built end effector including a digital light processor, optics, and camera, is mounted to the robot and can be positioned anywhere within a 20x20x20 cm work envelope (Figure 1b). The workpiece is placed on a kinematic mount attached to the rotary stage (Figure 1c). The measured repeatability and accuracy values of the motion system and thus the projected pattern are 20 and 30 microns, respectively. The resolution of the projected light pattern is approximately 1 micron.

The substrate is patterned by digitally triangulating an object with a 3D scanner (Figure 2a) and associating the location of each triangle in the digital space with that in real space. Each triangle is then associated with the computer-applied texture contained within its borders and stored in memory for later projection. The texture is then replicated on the photopolymer-coated substrate by sequentially exposing every triangle in the digital file (Figure 2b, 2c).

We present preliminary demonstrations of functionality by pattern transfer to a metal sphere via etching and by patterning hydrogel microstructures onto a small bone.

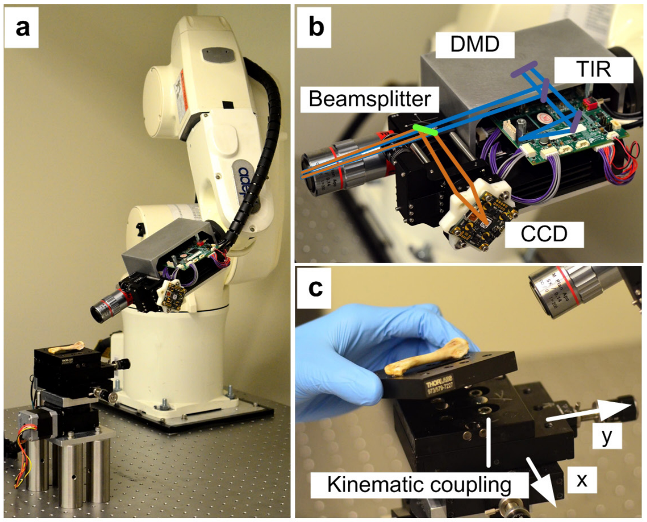

▲Figure 1 (left): Robotic photopatterning system. a) motion system comprising 6-axis robot and rotary stage; b) custom dynamic-mask projection end-effector; c) bone substrate mounted to kinematic coupling fixture.

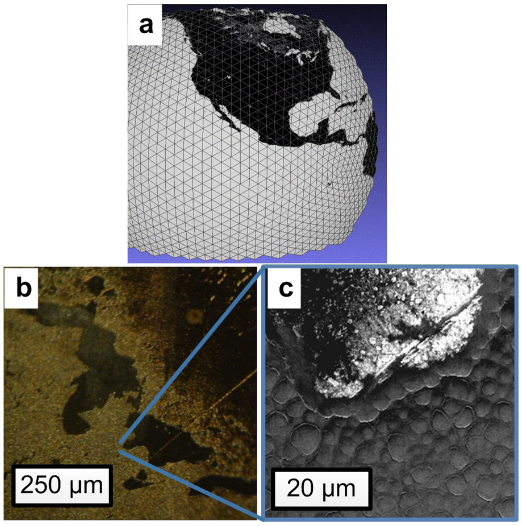

▲Figure 2 (right): Test patterning of a 3D surface. a) triangulation of a spherical surface with applied texture of North America; b) optical micrograph of sphere surface with texture replicated in photopolymer; c) electron micrograph of (b) showing microstructure of photopolymer after development.

FURTHER READING

- Y. L. Kong, I. Tamargo, H. Kim, B. Johnson, M. Gupta, T. Koh, H, Chin et al., "3D Printed Quantum Dot Light-Emitting Diodes," Nano Lett. doi:10.1021/nl5033292, 2014.
- Aiscent Technologies, "Spherical Surface Lithography Solutions. 1 (2012). at <http://www.aiscenttech.com/en/solutions/sphericallithography/>
- J. Kim M. Dadsetan, S. Ameenuddin, A.J. Windebank, M.J. Yaszemski, L. Lu, "In vivo biodegradation and biocompatibility of PEG/sebacic acid-based hydrogels using a cage implant system," *J. Biomed. Mater. Res. A*, vol. 95, pp. 191–7, 2010.

Application of Tungsten as a Carbon Sink for Synthesis of Uniform Monolayer Graphene free of Bilayers/Multilayers

W. Fang, A. Hsu, Y. Shin, Y. Song, T. Palacios, J. Kong
Sponsorship: National Science Foundation

Graphene has attracted great interest because of its exceptional physical properties and enormous potential for various electronic applications. Many synthesis methods have been developed to prepare high-throughput monolayer graphene including mechanical exfoliation, reduction of graphene oxide, SiC thermal decomposition and chemical vapor deposition (CVD). Among them, CVD is one of the most promising approaches because it allows for growth of high-quality large-area graphene, which later on can be easily transferred to arbitrary substrates. Currently, copper is most commonly used as a substrate for the CVD growth of monolayer graphene because of its low carbon solubility. Although the uniformity of graphene grown on copper is greatly improved as compared to that on nickel, small bilayer domains with size of 1~5 µm can still be observed. Moreover, researchers found that bilayer formation is highly dependent on the morphology and impurity of the Cu foil and growth conditions. Therefore, to achieve uniform monolayer graphene, various methods of pre-treating the copper foil have been studied such as etchant cleaning, chemical-electro polishing and many-hour annealing. The size of the bilayers can also be minimized, but not eliminated, by tuning the concentration of hydrogen.

In this work, we focus on graphene growth on Cu enclosures due to asymmetry of carbon delivery between the two surfaces. Our previous works have shown that by using Cu enclosures for growth, high coverage of bilayer graphene can be achieved on the outside surface of the enclosure because carbon inside can diffuse out to form bilayers on the outside. The carbon source diffusion process is driven by the concentration gradient across the copper foil. In this work, we propose that by reversing the direction of the carbon diffusion, we can selectively remove bi-/multi-layers to achieve uniform monolayer graphene. We utilize a tungsten foil, which acts as a carbon sink inside the enclosure.

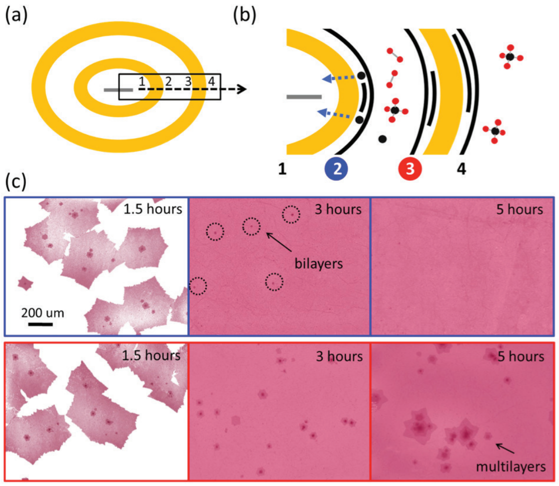

▲ Figure 1: Graphene grown on Cu double enclosures. (a) Schematics of the Cu double enclosures. (b) Growth mechanism for bi-/multi-layer graphene on surface 2 disappear while remains on surface 3. (c) Comparison of graphene grown on the surface 2 and 3 as a function of time.

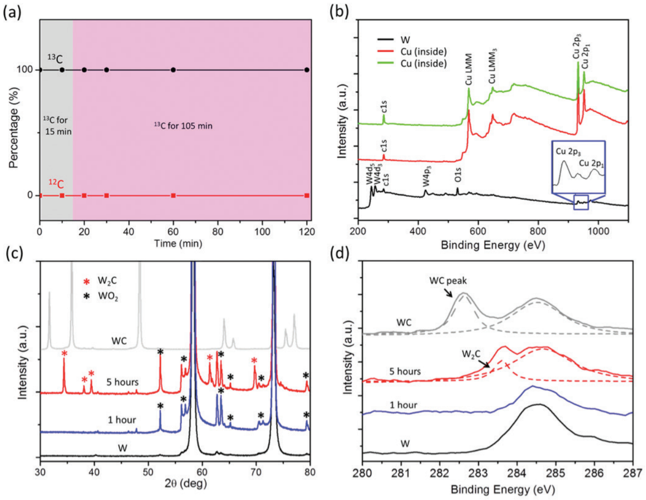

▲ Figure 2. Characterization of the graphene grown on Cu enclosures with tungsten and the composition analysis of the tungsten foil. (a) Percentage of ^{12}C and ^{13}C isotope in monolayer graphene. (b) XPS results and (c) XRD results on as-received tungsten foil (black), tungsten foil after 1-hour (blue) and 5-hour growth (red), and as-received tungsten carbide (grey). (d) Detailed XPS spectrum of C1s.

FURTHER READING

- A. K. Geim, "Graphene: Status and Prospects," *Science*, vol. 324, pp. 1530-1534, Jun. 19 2009.
- K. S. Novoselov, A. K. Geim, S. V. Morozov, D. Jiang, Y. Zhang, S. V. Dubonos, I. V. Grigorieva, and A. A. Firsov, "Electric field effect in atomically thin carbon films," *Science*, vol. 306, pp. 666-669, Oct. 22 2004.
- X. S. Li, W. W. Cai, J. H. An, S. Kim, J. Nah, D. X. Yang, R. Piner, A. Velamakanni, I. Jung, E. Tutuc, S. K. Banerjee, L. Colombo, and R. S. Ruoff, "Large-Area Synthesis of High-Quality and Uniform Graphene Films on Copper Foils," *Science*, vol. 324, pp. 1312-1314, Jun. 5 2009.

Roll-To-Roll Transfer of CVD-Grown Graphene onto Flexible Substrates Using Heated Roll Lamination and Electrochemical Delamination

M. Hempel, T. Palacios, J. Kong

Sponsorship: Eni S.p.A.

Since its extraction in 2004, graphene has attracted tremendous attention due to its unique properties such as single-atom thickness, mechanical strength, and extremely high carrier mobility. Additionally, this material is 98.7% transparent, very flexible, and easily doped. Owing to these characteristics, it is a promising candidate to replace indium-doped tin oxide (ITO) as transparent conductive film in future flexible optoelectronic applications. ITO is brittle and expensive, which makes it not well suited for low-cost optoelectronic devices such as flexible solar cells or displays that could be used in clothing or as electric papers. Driven by this motivation, the goal is to create a scalable technology to produce graphene on flexible, transparent substrates with a sheet resistance below 100 Ω/□ ,which is necessary for the presented applications.

In this work, we developed a setup (see Figure 2) to transfer graphene from copper foil directly onto polyethylene terephthalate (PET) films. A schematic of the setup is depicted in Figure 1. To facilitate the transfer, a graphene/copper strip is first laminated onto the PET film. The PET substrate is coated with a thin ethylene-vinyl acetate (EVA) layer. The heated rollers (130°C) melt the EVA to create a glue-like layer that bonds the PET film firmly to the graphene. Subsequently, the copper foil is electro-chemically delaminated in a sodium hydroxide bath (1 Mol/l). Applying a voltage between the copper and a platinum counter electrode, that is also submersed the electrolyte bath, generates hydrogen bubbles at the graphene/copper interface that gently separate the copper from the graphene/EVA/PET compound film. Lastly, the rewind stage collects the two films on individual rollers.

So far, we have demonstrated a graphene transfer from copper strips (W 1.2 cm, L 10 cm, H 25 µm) onto PET (75 µm) with a sheet resistance of 5 kΩ/□. In the future, we want to optimize the transfer parameters to lower the sheet resistance to reach the goal stated above and expand the transfer process to be continuous on meter-long substrates.

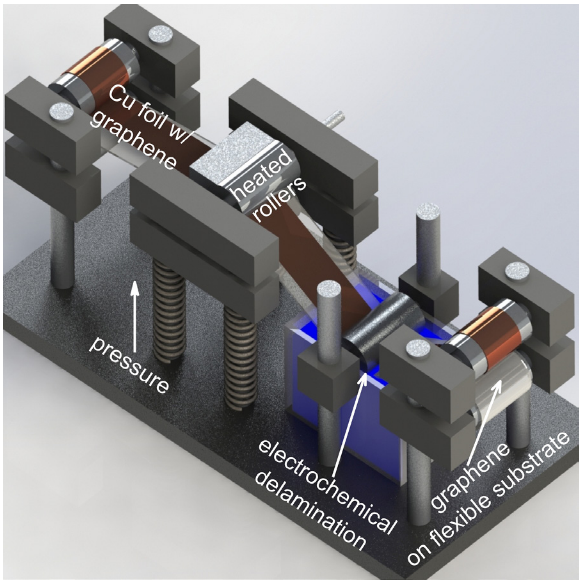

▲Figure 1: Schematic of developed roll-to-roll transfer setup. First, copper with graphene is laminated onto a PET/EVA substrate using pressure and heat. The copper is then electrochemically delaminated, leaving graphene on the PET/EVA substrate.

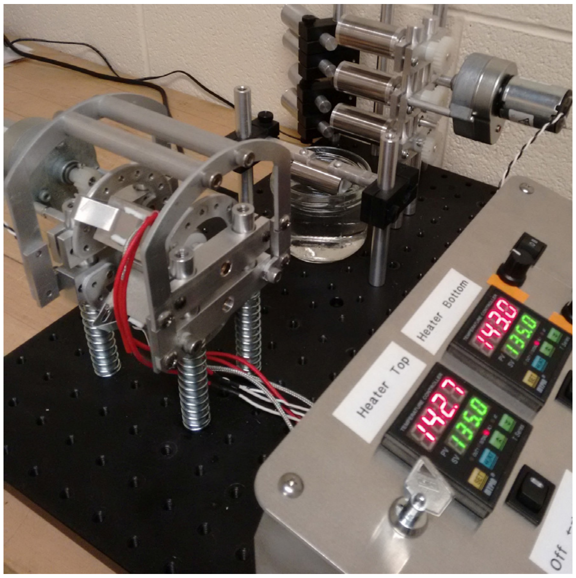

▲Figure 2: Actual implementation of setup. (Mid-left) lamination unit, (bottom right corner) control panel with temperature and motor speed control, and (top right corner) rewind stage with three rollers for graphene transfer from both copper sides.

FURTHER READING

- K. Rana, J. Singh, and J.-H. Ahn, "A graphene-based transparent electrode for use in flexible optoelectronic devices," *J. Mater. Chem. C*, vol. 2, pp. 2646-2656 Mar. 2014.
- S. Bae, H. Kim, Y. Lee, X. Xu, J.-S. Park, Y. Zheng, J. Balakrishnan, T. Lei, H. Ri Kim, Y. I. Song, Y.-J. Kim, K. S. Kim, B. Özyilmaz, J.-H. Ahn, B. H. Hong, and S. Iijima, "Roll-to-roll production of 30-inch graphene films for transparent electrodes," *Nat Nano*, vol. 5, no. 8, pp. 574–578, Aug. 2010.
- L. Gao, W. Ren, H. Xu, L. Jin, Z. Wang, T. Ma, L.-P. Ma, Z. Zhang, Q. Fu, L.-M. Peng, X. Bao, and H.-M. Cheng, "Repeated growth and bubbling transfer of graphene with millimetre-size single-crystal grains using platinum," *Nature Communications*, vol. 3, p. 699, Feb. 2012.

Integration of 2D Materials into 3D Printing

M. Aby, E. McVay, J. Addison, T. Palacios

Sponsorship: NASA, Office of Naval Research PECASE

In recent years, 3D printing has revolutionized how things are made. It is now used in all kinds of rapid prototyping as well as by hobbyists and companies to make finished products and can print not only plastic but also metal, ceramics, and even biological tissue. The next step towards expanding the capabilities of 3D printing technology is to be able to print electronics directly into the 3D structures, as opposed to having to add them in afterwards. Other groups have made some progress in printing conducting inks into and sintering metal onto the 3D structures, and some are working on using pick and place machines to be able to add electronic components directly. Our work seeks to complement this other work by adding the capability to directly print 2D materials such as graphene, MoS_2, and nanoparticle solutions in order to embed complete circuits (e.g., sensors, energy harvesters, or displays) directly into the 3D object.

Two-dimensional materials have showed amazing promise since their discovery, and devices from capacitors to transistors have been demonstrated with graphene, MoS_2, and other 2D-materials. At the same time, nanoparticle inks have also been used to create conductive traces and could potentially prove useful in creating energy storage devices as well. Building on previous work in our group on graphene-based inks and direct printing of graphene-based supercapacitors and strain sensors, this project aims to integrate these technologies into a 3D printer.

The printer we are using is a RepRap Mendel Max 1.5, a fully open-source printer that is relatively inexpensive and readily customizable. Our group has modified the printer hardware to allow for printing of 2D material inks and is working on software to integrate 2D circuits with slices of 3D models. The project aims to print conductive traces and nanoparticle inks including graphene, graphene oxide, and MoS_2 directly into 3D structures made of PLA and other types of plastic.

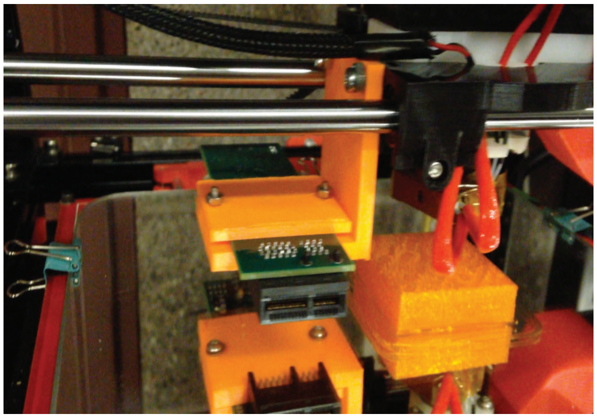

▲Figure 1: Screenshot from video of the printer printing PLA plastic (right) and graphene oxide ink (left) simultaneously. The green circuit board holds the electronics for the inkjet printerheads that print 2D materials.

▲Figure 2: Flexible capacitor made on PET from the laser reduction of graphene oxide. Devices like this could eventually be integrated directly into 3D printed structures for energy storage and delivery.

FURTHER READING

- M. F. El-Kady, V. Strong, S. Dubin, and R. B. Kaner, "Laser scribing of high-performance and flexible graphene-based electrochemical capacitors," *Science*, vol. 335, no. 6074, pp. 1326-1330, Mar. 2012.
- S. Wang, P. K. Ang, Z. Wang, A. L. L. Tang, J. T. L. Thong, and K. P. Loh, "High mobility, printable, and solution-processed graphene electronics," *Nano Letters*, vol. 10, pp. 92-98, Jan. 2010.
- M. Kaempgen, C. Chan, J. M. Y. Cui, and G. Gruner, "Printable thin film supercapacitors using single-walled carbon nanotubes," *Nano Letters, vol.* 9, pp. 1872-1876, May 2009.

Electrospray-Printed 2D Material Humidity Sensors

A. P. Taylor, L. F. Velásquez-García

Sponsorship: Edwards Vacuum

State-of-the-art conductometric gas sensors, based on semiconducting metal oxide films (MOXs), are widely used due to their simplicity and broad applicability to detect many species. However, only a few MOXs show an adequate combination of catalytic activity and thermodynamic stability for gas sensing; these MOXs need to be doped with noble metal nanoparticles to compensate for their poor gas sensitivity, which visibly increases their cost. Fabrication via electrohydrodynamic jetting has recently received attention as a promising candidate for production of low-cost micro- and nanosystems because of its capability to create thin films of high quality without the extreme conditions of standard semiconductor processing (i.e., high vacuum and/or high temperature).

An attractive substitute active material for chemical gas sensing is graphene oxide (GO) because of its high sensitivity to surface adsorbates and compatibility to harsh environments. Thin-film GO sensors have been fabricated with aqueous suspensions of GO flakes using drop casting, air-brush spraying, spin coating, and inkjet printing. Nonetheless, electrospray printing of GO thin-film sensors offers more precise control of the film properties than the other techniques and can also lower production costs through emitter multiplexing. We manufactured GO sensors at low temperatures (< 100 °C) with average layer thickness around 60 nm and characterized their response to humidity in an environmental chamber.

We fabricated devices with multiple electrode configurations on SiO_2-coated Si wafers using contact photolithography and the lift-off technique, and electrosprayed a thin film of GO through a shadow mask onto the electrode structures to form the sensors. We then gold wire-bonded the completed sensor chips into standard IC packages (Figure 1) and placed our GO sensors along with a commercially available humidity sensor (Honeywell HIH-4000) inside an environmental chamber and varied the humidity. A data logger recorded the change in resistance of the GO sensor (Figure 2 top, red curve) and the response of the commercial sensor (Figure 2 top, black curve); the two data sets tracked each other closely. The change in humidity shows a quadratic behavior with the change in resistance of the GO sensor (Figure 2 bottom) where $\Delta R/R_0=(R_{1243}-R_0)/R_0$ and $R_0=39k\Omega$. The results were reproducible on different days, and the GO sensors showed no signs of degradation after storage for more than one month.

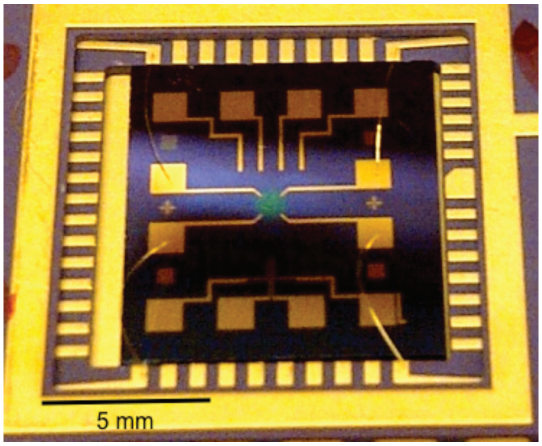

▲ Figure 1: Electrospray-printed GO sensor (greenish dot at center) on top of Au electrodes in the Van der Pauw configuration.

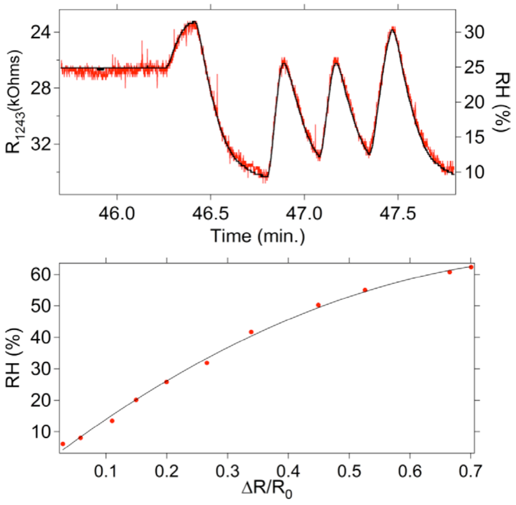

▲ Figure 2: GO sensor response to humidity (red) compared with a commercially available sensor (top) and relative humidity as a function of the sensor response (bottom).

FURTHER READING

- P. Ponce de Leon, F. A. Hill, E. V. Heubel, and L. F. Velásquez-García, "Parallel Nanomanufacturing via Electrohydrodynamic Jetting from Microfabricated Externally-Fed Emitter Arrays," *Nanotechnology*, vol. 26, no. 22, 225301 (10 pp.), June 2015.
- F. A. Hill, E. V. Heubel, P. Ponce de Leon, and L. F. Velásquez-García, "High-Throughput Ionic Liquid Ion Sources Using Arrays of Microfabricated Electrospray Emitters with Integrated Extractor Grid and Carbon Nanotube Flow Control Structures," *Journal of Microelectromechanical Systems*, vol. 23, no. 5, pp. 1237-1248, Oct. 2014.
- A. P. Taylor and L. F. Velásquez-García, "Electrospray-Printed Graphene Oxide Nanostructured Gas Sensors," in preparation.

Quantitative Analysis and Modeling of Templated Solid-State Dewetting of Thin Single-Crystal Ni Films

G. H. Kim, R. V. Zucker, Y. A. Shin, W. C. Carter, C. V. Thompson

Sponsorship: National Science Foundation

Thin films are generally metastable in the as-deposited state and will dewet (agglomerate) when heated. Nanometer-scale films (<100 nm thick) can dewet at temperatures well below the melting temperature of the film, and dewetting occurs while the film remains solid. This phenomenon can limit the use of very thin films in microsystems, but it can also be used to controllably produce complex structures. Dewetting occurs through retraction of the edges of naturally forming holes or at patterned edges of films. In single-crystal films, anisotropy in surface energy and diffusivity drives the dewetting process to result in regular patterns that relate to the crystal symmetry. We are investigating use of anisotropic dewetting as a self-assembly method to generate complex, small, predetermined patterns (Figure 1). A quantitative understanding of dewetting mechanisms is critical for design of self-assembled structures made through dewetting. We studied the Rayleigh-like instability of long strips patterned on single crystal Ni films. These long strips dewet to form wire-like structures, which eventually break-up into islands, similar to the Rayleigh instability of free-standing cylinders. We found that the characteristic spacing of the dewetted islands and the dewetting rate are highly anisotropic and the spacing is dependent on the total surface energy of the wires (Figure 2). Additionally, a kinetic Monte Carlo simulation has been carried out to test our understanding of dewetting mechanisms. This model provides good agreement with experimental observations. We are also developing a three-dimensional phase-field model for dewetting of materials with isotropic and/or anisotropic surface energies.

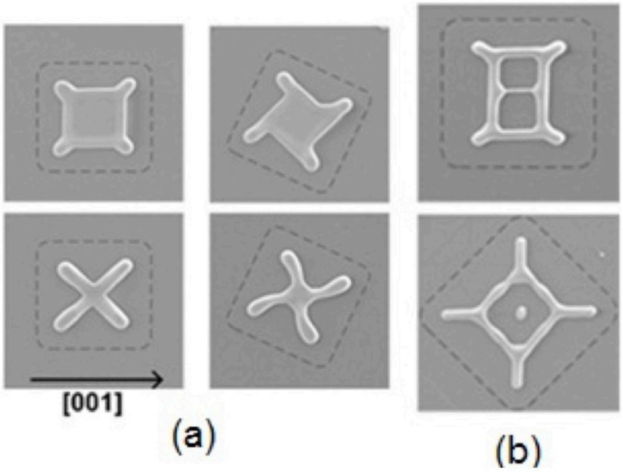

▲ Figure 1: (a) Partially dewetted patches patterned from a (100) film into squares with different in-plane orientations; top is an earlier time than bottom. (b) Dewetting patterns of larger squares.

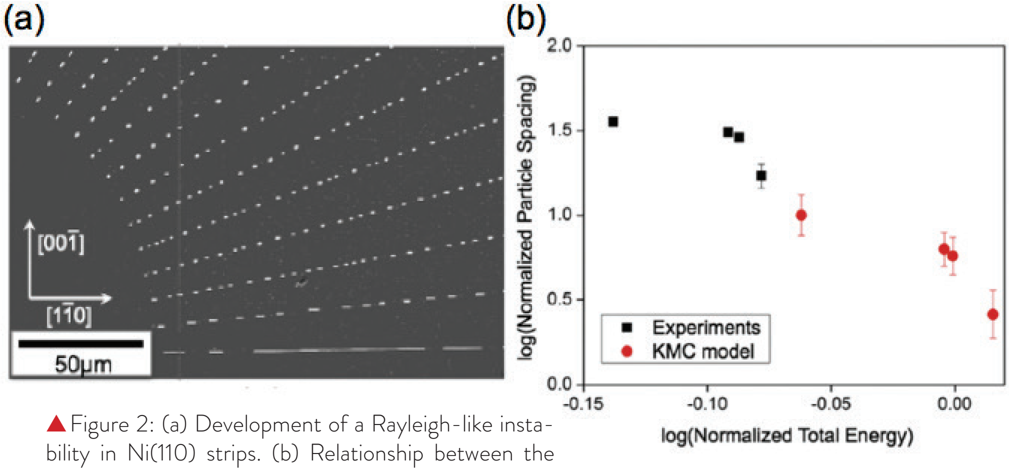

▲ Figure 2: (a) Development of a Rayleigh-like instability in Ni(110) strips. (b) Relationship between the particle spacing as a function of the total surface energy of the wire.

FURTHER READING

- J. P. Ye and C. V. Thompson, "Templated solid state dewetting to controllably produce complex patterns," *Advanced Materials*, vol. 23, pp. 1567-1571, 2011.
- G. H. Kim and C. V. Thompson, "Effect of surface energy anisotropy on Rayleigh-like solid-state dewetting and wire stability," *Acta Materialia*, vol. 84, 2015.
- W. Jiang, W. Bao, C. V. Thompson, and D. J. Srolovitz, "Phase Field Approach for Simulating Solid-State Dewetting Problems," *Acta Materialia* vol. 60, pp. 5578–5592, 2012.

Metal-Assisted Chemical and Anodic Etching to Form Arrays of Silicon Nanostructures

W. Zheng, C. Q. Lai, P. Lianto, W. K. Choi, C. V. Thompson
Sponsorship: Singapore-MIT Alliance for Research and Technology

Metal-assisted chemical etching (MACE) has been used to fabricate a wide array of semiconductor nanostructures using a room temperature wet etching process. These include arrays of nanowires with diameters down to 20 nm and aspect ratios as high as 220 to 1 (Figure 1). In a typical MACE process, a metal film is deposited on silicon, patterned, and exposed to an etchant consisting of HF and an oxidant (e.g., H_2O_2). The metal catalyzes reduction of the oxidant and provides an electronic hole for oxidation of silicon to form a soluble reaction product. This process causes etching of the Si at the metal/Si interface, and results in the controlled formation of un-etched silicon nanostructures. Beyond this point, the detailed mechanisms of MACE have remained unclear. This lack of knowledge has inhibited extension of the use of this technique to a wider range of semiconductors.

In addition to using the MACE process to fabricate sensors, microbatteries, and supercapacitors (discussed elsewhere), we have carried out basic research on the mechanisms of MACE. In recent work, we etched mechanically supported metal strips to measure the forces that keep the metal and silicon in contact during etching, and identified them as Hamaker forces. We have also shown how these forces depend on the chemistry of the etchant. In addition, we have clarified the role of excess holes in causing porosity in the resulting nanostructures and shown that application of an external electric field can be used to control porosity.

In the past year, we have demonstrated a new electrochemical method for formation of arrays of silicon nanostructures, metal-assisted anodic etching (MAAE). In this process, the etchant consists of HF alone and does not include an oxidant. Holes are supplied through an external circuit, with anodic contact to either the metal or the silicon (Figure 2). In both cases, the metal still catalyzes the etching process and leads to controlled formation of arrays of nanostructures (such as nanowire). This discovery, and its analysis, provide new flexibility in the use of metal catalyzed electrochemical etching, and also provides new insights into the mechanisms of both MAAE and MACE.

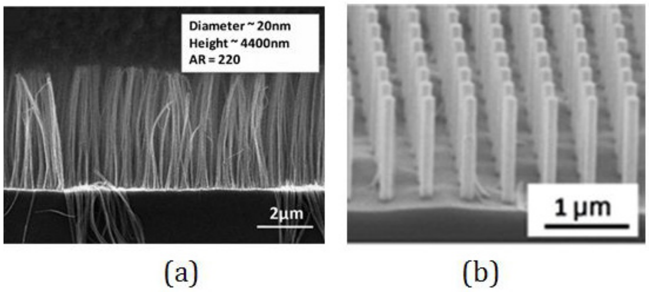

▲ Figure 1: Silicon nanowire array made using MACE with metal films patterned using (a) block copolymer lithography and (b) interference lithography.

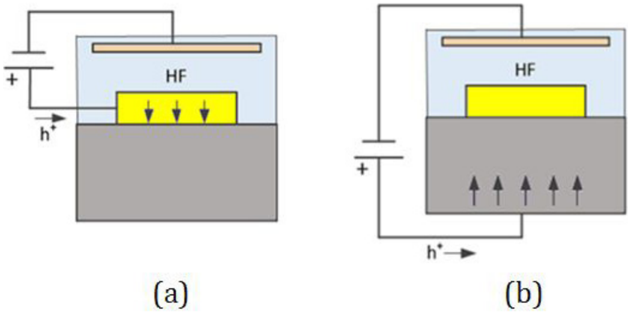

▲ Figure 2: Configurations for metal-assisted anodic etching (MAAE) with (a) anodic contact to the metal, and (b) anodic contact to the silicon.

FURTHER READING

- P. Lianto, S. Yu, J. Wu, C. V. Thompson and W. K. Choi, "Vertical Etching with Isolated Catalysts in Metal-Assisted Chemical Etching of Silicon," *Nanoscale*, vol. 4, pp. 7532, 2012.
- C. Q. Lai, H. Cheng, W. K. Choi, and C. V. Thompson, "Mechanics of Catalyst Motion During Metal-Assisted Chemical Etching of Silicon," *The Journal of Physical Chemistry C*, vol. 117, pp. 20802, 2013.
- C. Q. Lai, W. Zheng, W. K. Choi, C. V. Thompson, "Metal Assisted Anodic Etching of Silicon," *Nanoscale*, no. 25, pp. 11123-11134, July 2015.

Thermal Conductivity Spectroscopy Using Nanostructures

L. Zeng, K. C. Collins, Y. Hu, M. N. Luckyanova, S. Huberman, V. Chiloyan, G. Chen
Sponsorship: S3TEC, Department of Energy

A material's ability to conduct heat is measured by its thermal conductivity. In semiconductors and dielectrics, the predominant heat carriers are quantized lattice vibrations (or phonons), which have a wide range of frequencies and mean free paths (MFPs). The mean free path of each phonon mode decribes the average distance that specific phonon mode travels in between two consecutive scattering events. The thermal conductivity accumulation function describes the fraction of the contribution of phonons with MFPs shorter than a cutoff MFP. The Nanoengineering Laboratory in MIT's Department of Mechanical Engineering hosts a femto-second laser pump-probe system to measure thermal conductivity of bulk materials and thin films, as well as interfacial thermal resistance. Currently, this system is being advanced to measure phonon MFP distributions in different materials.

The idea of probing phonon MFP distribution is based on examining heat transport in the quasiballistic regime that occurs when characteristic heat source sizes are comparable with phonon MFPs. We first observed quasiballistic phonon transport in crystalline sililcon at cryogenic temperatures when the phonon MFPs are longer than the laser beam diameters that determine the size of the heat source. This observation led to the idea of mapping out phonon MFP distributions by systematically changing the size of the heat source. Since phonon MFPs in many materials span sizes from several nanometers to hundreds of microns, one nontrivial challenge is to create nanometer scale heat sources comparable to the phonon MFPs. We fabricated nanostructures, subjected them to laser heating as heat sources, and developed techniques to distribute phonon MFPs in different materials such as GaAs and GaN. Now, we are simplifying the technique using 1D metallic gratings. The metal lines serve as heaters and thermometers. Our experimental observation that when the heat source size is smaller than the phonon MFPs, the classical Fourier heat conduction theory underpredicts the temperature rise also has significant implications for thermal management in microelectronic devices.

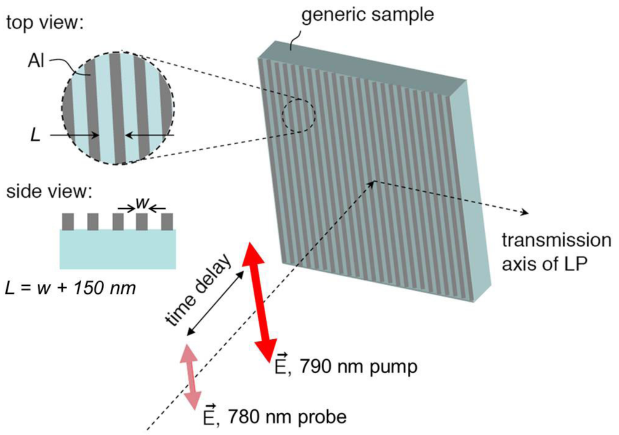

▲Figure 1: Schematic of our sample structures and experimental technique. The samples are composed of metal grating on top of substrates of interests and are measured by an ultrafast optical time-domain thermoreflectance technique in the RK lab at MIT.

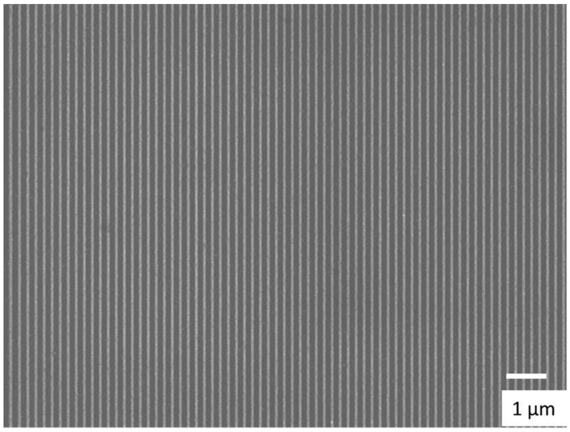

▲Figure 2: Fabricated 50-nm-wide (period = 200 nm) one-dimensional aluminum metal grating on top of crystalline silicon substrate using the ebeam machine Elionix in the Microsystems Technology Laboratory at MIT.

FURTHER READING

- A. J. Minnich, J. A. Johnson, A. J. Schmidt, K. Esfarjani, M. S. Dresselhaus, K. A. Nelson, and G. Chen, "Thermal conductivity spectroscopy technique to measure phonon mean free paths," *Physical Review Letters*, vol. 107, p. 095901, 2011.
- L. Zeng and G. Chen, "Disparate Quasiballistic Heat Conduction Regimes from Periodic Heat Sources on a Substrate," *Journal of Applied Physics*, vol. 116, p. 064307, 2014.
- Y. Hu, L. Zeng, A. J. Minnich, M. S. Dresselhaus, and G. Chen, "Spectral Mapping of Thermal Conductivity through Nanoscale Ballistic Transport," *Nature Nanotechnology*, June 2015, http://dx.doi.org/10.1038/nnano.2015.109.

Inducing Superconductivity in Semiconducting Atomically Thin Layers

E. Navarro-Moratalla, P. Jarillo-Herrero

Sponsorship: CIQM, Ramon Areces Foundation

The combination of semiconducting transition metal dichalcogenides—chemical formula MX_2, with M: Mo, W; and X: S or Se—with modern nanofabrication techniques (exfoliation and van der Waals stacking) has paved the way for the realization of extremely clean two-dimensional electronic systems, so that unprecedented physical properties can now be observed. In particular, the Mo chalcogenides have recently drawn attention due to the occurrence of superconductivity by accumulation of a high density of electrons at their surface. Although the induction of superconductivity has been achieved in bulk crystals and thick flakes, no similar studies in atomically thin layers have appeared. Particularly appealing is the case of single-layer systems where the breaking of the inversion symmetry in single layers in addition to a strong spin-orbit coupling could provide access to the valley degree of freedom within the superconducting state. This access could give rise to exotic phenomena such as unconventional Andreev reflection or superconducting spin valves.

Instrumental to the generation of a high carrier density is the electrical double layer technique, which involves the use of an ionic liquid top gate. However, the use of a liquid imposes several technical challenges. First, it freezes as the device is cooled down, generating mechanical stress. Second, it exhibits a strong chemical reactivity with standard metallic contacts. This problematic prevents the normal characterization of the physical properties down to base temperature. In addition, working on Si/SiO_2 substrates implies the presence of charged surface states and electron/hole puddles. This presence has been found to limit the sample quality and reduce the carrier mobility.

Both problems were tackled by using a new fabrication approach. MoS_2 single layers were exfoliated on top of a thin film of polymer. A layer was selected and transferred onto Au contacts pre-evaporated on an h-BN surface (see Figure 1a). The current strategy improves the performance of the final devices with respect to standard evaporated contacts: it isolates the metal contacts from the chemical corrosion of the liquid; the h-BN provides a defect-free surface; and the polymer film serves as a strain-relieving buffer interface. As a result, the devices fabricated have been successfully characterized to temperatures below 1 K and exhibit low ohmic contact resistances and maximum Hall mobilities of over 900 cm²/Vs measured at 4 K (see Figure 2).

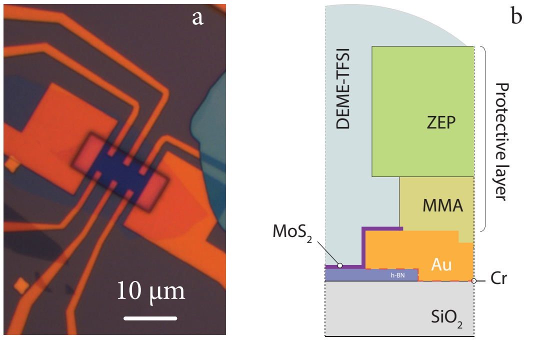

▲ Figure 1: (a) Optical micrograph of a single-layer MoS_2 EDL device. Rectangular frame around device's transport channel is a hole in protective MMA layer. (b) Scheme showing multilayer cross-section of device shown in (a) including ionic liquid (DEME-TFSI).

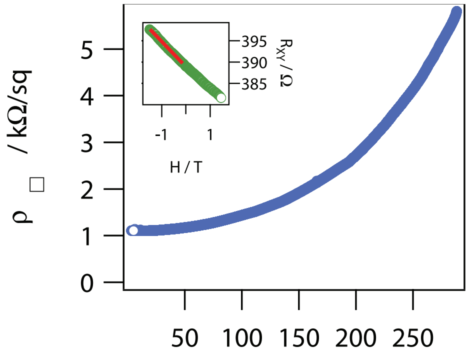

▲ Figure 2: Four-probe transport properties measured at ionic liquid gate voltage V_{ion} = 1.3 V. Inset shows Hall resistance as a function of external applied field. Linear fit provides a mobility of 907.4 cm²/Vs @ 4 K for carrier density of $1x10^{14}$ cm^{-2}.

FURTHER READING

- J. T. Ye, Y. J. Zhang, R. Akashi, M. S. Bahramy, R. Arita, and Y. Iwasa, "Superconducting dome in a gate-tuned band insulator," *Science*, vol. 338,no. 6111, pp. 1193–1196, Nov. 2012.
- Y. Ge and A. Y. Liu, "Phonon-mediated superconductivity in electron-doped single-layer MoS_2: A first-principles prediction," *Physical Review B - Condensed Matter and Materials Physics*, vol. 87, pp. 241408(R), Jun. 2013.

Electrostatic Coupling between Two Surfaces of a Topological Insulator

V. Fatemi, B. Hunt, H. Steinberg, S. L. Eltinge, F. Mahmood, N. P. Butch, K. Watanabe, T. Taniguchi, N. Gedik, R. C. Ashoori, P. Jarillo-Herrero

Sponsorship: Department of Energy, Moore Foundation, National Science Foundation

Topological insulators have been undergoing intense theoretical and experimental research on the properties of their unique surface electronic states. The presence of bulk carriers has hampered experimental progress, so a large variety of growth techniques and device structures have been implemented in the attempt to access a surface-state dominated regime. For example, quaternary compounds of the form $Bi_{2-x}Sb_xTe_{3-y}Se_y$ have a significantly suppressed bulk contribution to transport and so are good candidates for surface-state dominated transport in nanoscale devices.

Here we report our successful *in situ* identification of two surface states on a single crystal of $Bi_{1.5}Sb_{0.5}Te_{1.7}Se_{1.3}$ as well as clear electric field penetration through the bulk, indicating full bulk suppression and surface-state dominance. In Figures 1a-b we show typical gating characteristics of the resistance. We see two distinct resistance peaks that are modulated by both gate voltages, which is strong evidence for two distinct surface states contributing to the electronic transport of the system. Additionally, this modulation provides evidence for electric field penetration; otherwise, the back-gate electrode could not affect the upper surface state. To understand the motion of the resistance peaks quantitatively, we developed an electrostatic charging model represented in Figure 1c, details of which can be found in the further reading references. Applying this model to the resistance peak allows for a linear transformation from gate voltages to chemical potential and carrier density. Figure 1d is a zoom-in of the motion of the upper surface resistance peak as a function of both gate voltages, and we find an excellent fit of the transport data to independently taken angle-resolved photoemission spectroscopy data of the surface state dispersion (Figure 1e), showing that our system is indeed surface-state dominated.

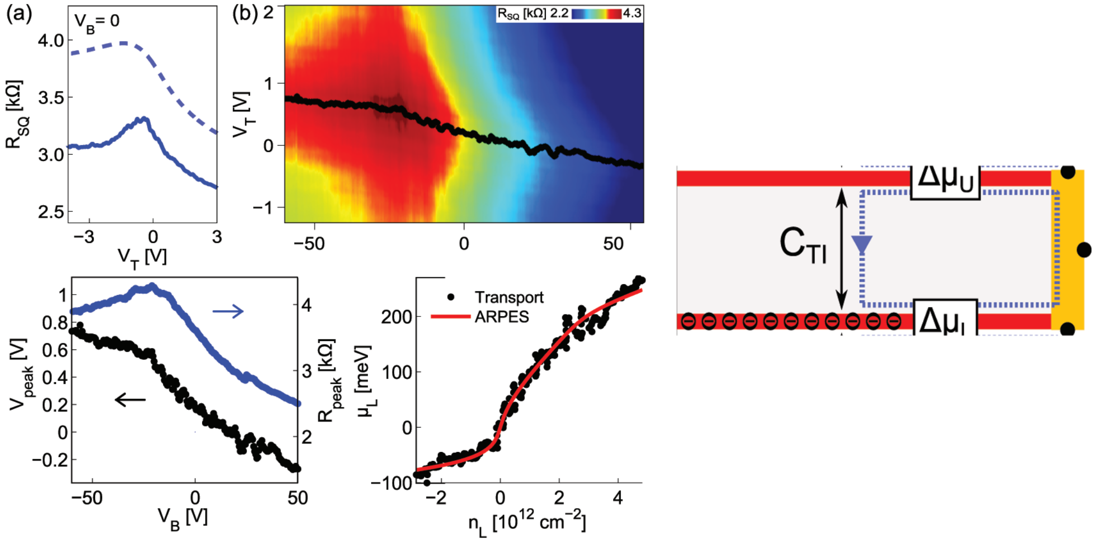

▲Figure 1: (a) Resistance vs. gate-voltage trace. Solid and dashed lines are at 4K and room temperature, respectively. (b) Resistance vs. top and bottom gate voltages. Black dots mark the upper surface resistance peak. (c) A schematic of the electrostatic charging model. (d) A close-up of the trajectory of the resistance peak from Figure 1b (black) and the resistance along that trace (blue). (e) Fit of transport-extracted dispersion relationship (black) to independently measured spectroscopy (red).

FURTHER READING

- V. Fatemi, B. Hunt, H. Steinberg, S. L. Eltinge, F. Mahmood, N. P. Butch, K. Watanabe, et al., "Electrostatic Coupling between Two Surfaces of a Topological Insulator Nanodevice," *Physical Review Letters*, vol. 113, no. 20 p. 206801, Nov. 2014.
- M. Z. Hasan and C. L. Kane. "Colloquium: Topological Insulators," *Reviews of Modern Physics*, vol. 82, no. 4, pp. 3045–3067, Nov. 2010. doi:10.1103/RevModPhys.82.3045.